ADVANCED THEORY AND SIMULATIONS
www.advtheorysimul.com

Hydrocracking of Naphthalene by $NiMo_3S_4$/ZSM-5 Catalyst: A Theoretical Study on the Reaction Mechanism

Wei Sun, Zichang Zhang, Xiaobing Kong, Chunguang Zhang, Shuanglin Yu, Anyuan Cao, Yuansheng Zhao,* and Qian Wang**

The study for effective utilization and conversion of polycyclic aromatic hydrocarbons in heavy oil of petroleum is of great significance in the chemical industry. Although extensive experiments have been conducted on the relevant catalyst performance and reaction conditions in the practical hydrocracking process, the reaction mechanism remains unclear. Here, a first-principles study is performed to address this long-standing issue by taking a polycyclic aromatic naphthalene molecule as an example and choosing a typical $NiMo_3S_4$/ZSM-5 bi-functional catalyst for the hydrocracking reaction. By comparing the performance of various crystal planes, it is identified that the (001) plane of $NiMo_3S_4$ and the (010) plane of ZSM-5 are the most effective crystal planes for the hydrogenation and cracking processes, respectively. Based on this catalytic structure, an optimal hydrogenation pathway from naphthalene to tetralin ($1\alpha \rightarrow 4\alpha \rightarrow 2\beta \rightarrow 3\beta$) is first revealed with the third hydrogen-addition stage as the rate-determining step. Then, it is disclosed that the cracking reaction occurs in the form of isomerization and energetically more favorable ring-opening mode, and the main products are determined to include toluene, ethylbenzene, benzene, ethane, and methane. These results would deepen our understanding of the hydrocracking of naphthalene to tetralin and other products, and further promote the research of reaction mechanisms and more efficient catalysts for the utilization of polycyclic aromatic hydrocarbons in heavy oil of petroleum.

1. Introduction

Petroleum, as a very important resource, plays an integral role in our daily lives, social progress, and economic development. However, the composition of petroleum is very complex, and the high content of polycyclic aromatic hydrocarbon mixtures in heavy oil makes it difficult to be directly processed and utilized.[1] Through hydrocracking, these large molecular compounds can be converted into smaller and lighter hydrocarbons, which can not only improve the overall conversion rate and value of heavy oil, but also yield more useful light fuels and chemicals, such as gasoline, diesel, light olefins, and aromatics.[2–4] Therefore, heavy oil hydrocracking has been one of the important subjects in both industry and academia, thus receiving extensive attention. As shown in **Figure 1**, the schematic diagram illustrates the entire hydrocracking steps and process. In the experiment, the catalyst is first put into a reaction kettle full of H_2 gas, and the heavy oil is then introduced, where the heavy oil interacts with the catalyst and H_2 gas, undergoing the hydrocracking reaction at ≈400 °C and 4 MPa. Theoretically, the hydrocracking reaction can be considered as a combined hydrogenation and catalytic cracking process. Hydrogenation, which typically occurs on the surface of transitional metals like Ni and Mo, saturates the unsaturated bonds of reactants and products, enabling C—C bonds more prone to breaking during the subsequent cracking stage. In the next step, catalytic cracking, induced by acidic centers from metal oxides, decomposes the complex ring-loop or long-chain structures into small simple molecules. Because different catalysts are required for the different stages, bi-functional catalysts consisting of metals and zeolites have been extensively studied.

The existing studies on the hydrocracking of polycyclic aromatic hydrocarbons can be grouped into three categories as summarized in **Table 1**: 1) most research focuses on the structure-activity relationship of catalysts, 2) some studies explore the impact of reaction conditions, and 3) a limited number of studies proposes reaction pathways and overall hydrocracking networks. For instance, in terms of the structure-activity relationship of catalysts, the hydrocracking of naphthalene, hydrogenation-resulted tetralin or decalin over different kinds of catalysts supported on different types of zeolites has been experimentally studied with a focus on the overall reaction activity and product selectivity.[5–10] It has been found that the complex polycyclic aromatic 1-methylnaphthalene can be converted into

W. Sun, Z. Zhang, X. Kong, A. Cao, Q. Wang
School of Materials Science and Engineering
Peking University
Beijing 100871, P. R. China
E-mail: anyuan@pku.edu.cn; qianwang2@pku.edu.cn

C. Zhang, S. Yu, Y. Zhao
Petrochemical Research Institute
PetroChina Company Limited
Block A42 Science Base PetroChina, Shahe Town, Changping, Beijing 102206, P. R. China
E-mail: zhaoyuansheng@petrochina.com.cn

The ORCID identification number(s) for the author(s) of this article can be found under https://doi.org/10.1002/adts.202500209

DOI: 10.1002/adts.202500209

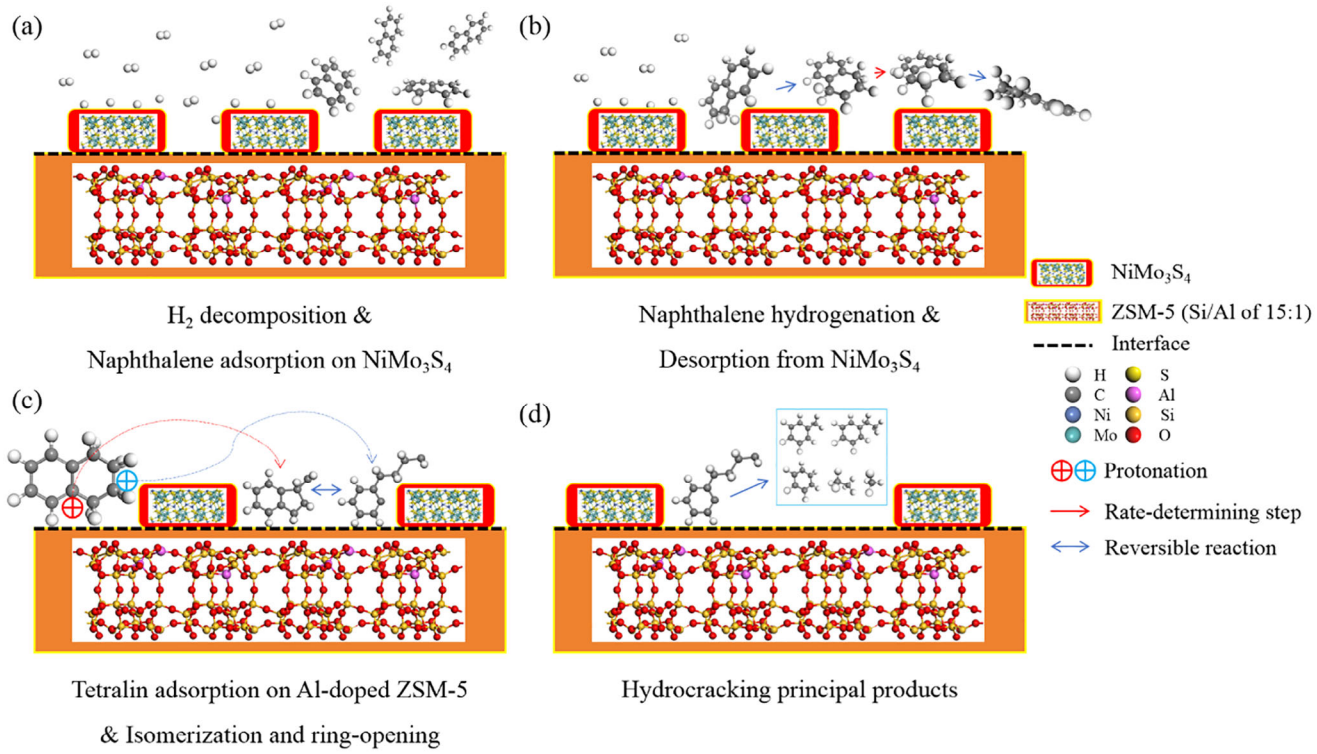

Figure 1. Hydrocracking steps and process of polycyclic aromatic hydrocarbons on a $NiMo_3S_4$/ZSM-5 bi-functional catalyst. a) H_2 gas decomposes and organic molecules being adsorbed on the surface of a metal catalyst. b) Reactive H atoms hydrogenate the empty orbitals of organic molecules, resulting in saturated molecules that subsequently desorb from the surface of metal catalysts. c) Saturated organic molecules adsorb on the zeolite surface and protonate to generate carbenium ions. d) Continuous cracking and hydrogenation of intermediates lead to final principal products.

Table 1. Summary of research work related to hydrocracking of polycyclic aromatic hydrocarbons.

Category	Detail	Reference
Structure-activity relationship of catalysts	Tetralin hydrocracking on K-modified Pt/USY catalysts	[5]
	Naphthalene hydrocracking over Mo_2C/HY catalysts	[6]
	Naphthalene, tetralin, and decalin over Pd/HY catalysts	[7]
	Tetralin over the NiMo sulfide catalysts supported on different types of zeolites	[8]
	Co-promoted Mo/β-zeolite for selective hydrocracking of tetralin and pyrolysis fuel	[9]
	Hydrocracking 1-methylnaphthalene to BTEX catalyzed by the β-zeolite supported Ni_2P	[11]
	Composite catalyst of Pt/Cr_2O_3-ZrO_2 for hydrocracking isopropylbenzene, 1,4-diisopropylbenzene, and 1,3,5-triisopropylbenzene	[12]
	Pyrolysis fuel oil into benzene, toluene, and xylene over CoMo/β-zeolite catalyst	[13]
	Efficient conversion of light cycle oil from fluid catalytic cracking to produce high-octane number gasoline	[14]
	Hydrocracking of fused aromatic hydrocarbons 9,10-dihydroanthracene catalyzed by Al-substituted HZSM-5	[15]
Influence of reaction conditions	Different temperature leading to different hydrocracking directions of tetralin experimentally	[10]
	Effect of reaction temperature and hydrogen pressure on slurry hydrocracking reactions of naphthalene	[16]
	Chemical reaction equilibrium of naphthalene and phenanthrene under the effect of inhibitors	[17]
	Effect of the pore topology of several zeolites on the cracking of tetralin and decalin	[18]
	Effects of zeolite topology and metal element doping on the hydrocracking performance of some polycyclic aromatic hydrocarbons	[19,20]
Reaction pathways and hydrocracking networks	Overall reaction network of tetralin hydrocracking depending on temperature experimentally	[10]
	Major hydrocracking reaction pathways of tetralin over bi-functional NiW/USY zeolite catalysts	[21]
	Major reaction pathways of tetralin hydrocracking over bi-functional Ir/SiO_2-Al_2O_3 catalysts	[22]
	Possible pathways and potential intermediates for the hydrocracking of dihydrophenanthrene experimentally	[23]

benzene, toluene, and xylene in the hydrocracking reactions catalyzed by the β-zeolite supported Ni_2P.[11] Moreover, the catalytic activity and reaction performance can be enhanced by introducing a composite catalyst like Pt/Cr_2O_3-ZrO_2 for hydrocracking isopropylbenzene, 1,4-diisopropylbenzene, and 1,3,5-triisopropylbenzene.[12] The hydrocracking of the mixture of pyrolysis fuel oil into benzene, toluene, and xylene over CoMo/beta zeolite catalyst has also been carried out experimentally.[13] More complex situations like efficient conversion of light cycle oil from fluid catalytic cracking[14] or hydrocracking of fused aromatic hydrocarbons 9,10-dihydroanthracene[15] have been explored theoretically. In addition, the influence of external and internal reaction conditions has also been studied, revealing that different hydrogenation pressures and reaction temperatures can control the pathways for hydrocracking naphthalene and tetralin.[10,16] The chemical reaction equilibrium of naphthalene and phenanthrene under inhibitors has been investigated through detailed kinetic studies.[17] By using probe molecules, the effect of the pore topology of several zeolites on the cracking of tetralin and decalin has been theoretically explored.[18] In the experiments, the relevant effects of zeolite topology and metal element doping on the hydrocracking performance of some polycyclic aromatic hydrocarbons have also been explored.[19,20] In addition, a few studies have been reported to reveal hydrocracking reaction networks. For example, the major hydrocracking reaction pathways have been presented in the form of a mechanistic scheme for tetralin on bi-functional catalysts such as NiW/USY zeolite[21] and Ir/SiO_2-Al_2O_3.[22] The temperature dependence of the overall reaction network of tetralin hydrocracking has been experimentally studied.[10] Very recently, the possible pathways and potential intermediates have been experimentally studied for the hydrocracking of dihydrophenanthrene under mild conditions.[23] However, despite significant progress made in both experimental research and theoretical study, the underlying mechanisms for hydrogenation sequence, rate-determining step, and potential cracking intermediates are not yet fully understood. Hence, in this work, taking the seminal polycyclic aromatic hydrocarbon naphthalene[24,25] as an example, we conduct a detailed theoretical study to elucidate the related mechanisms.

For hydrogen evolution, transition metal chalcogenides (TMC) have been found to be one kind of the most representative and hierarchical catalysts.[26–29] It has been reported that the electrocatalytic activity of TMC can be effectively enhanced by introducing different 3*d* transition metal elements to increase the *d*-electron density,[30] as is the case with $NiMo_3S_4$, which exhibits high efficiency as an electrocatalyst for water splitting[31,32] and for hydrogen evolution.[33] Therefore, we choose $NiMo_3S_4$ as the catalyst for the hydrogenation of naphthalene in this work. Furthermore, it has been found that zeolite catalysts can be used for converting polyaromatic hydrocarbons into benzene, toluene, ethylbenzene, and xylene (BTEX) due to their unique geometric structures with suitable pore size and moderate acidity strength.[9,34,35] Especially, zeolite socony mobil-5 (ZSM-5) material has been found to exhibit outstanding performance in aromatics hydrocracking,[36] methanol conversion,[37] and paraffin dehydrogenation[38] due to its multi-lamellar structure, high mesoporosity, and abundant acidic catalytic centers when Al atoms introduced.[39] Therefore, we choose it as our cracking catalyst for hydrocracking naphthalene.

As the simplest polycyclic aromatic hydrocarbon, naphthalene is worthy to mention that it can be hydrogenated into two intermediates, tetralin, and decalin during the hydrocracking process.[40] However, decalin is much more difficult to obtain due to the tendency of forming tetralin and the difficulty of dearomatizing its stable aromatic ring.[41,42] Therefore, our focus is on the reaction pathway from naphthalene to tetralin, and subsequently to the related products.

2. Computational Methods

Our calculations are carried out based on the density functional theory (DFT) and the projector augmented wave (PAW) method[43,44] as implemented in the Vienna ab initio simulation package (VASP).[45] The generalized gradient approximation (GGA)[46] with the Perdew–Burke–Ernzerhof (PBE) functional[47] is used to account for the exchange-correlation potential of electrons for geometry optimization. The plane waves with a kinetic energy cutoff of 500 eV are used to expand the wavefunction of valence electrons. The convergence thresholds of 10^{-4} eV and 10^{-2} eVÅ^{-1} are set for the total energy and force, respectively. The Brillouin zone is represented by using $3 \times 3 \times 3$ Monkhorst-Pack *k*-meshes.[48] Slab models of $NiMo_3S_4$ (001) and ZSM-5 (010) surfaces with $2 \times 2 \times 2$ supercells are generated from the Materials Project (MP) Database,[49] where the atoms in the bottom five atomic layers are fixed at their bulk positions, while the atoms in the top five layers are fully relaxed to simulate the surface phases of the catalysts. To mitigate interactions between repeating slabs, a vacuum space of 15 and 20 Å is added in the *z*-direction, respectively. The Ewald energy method implemented in the pymatgen software[50,51] is applied to generate a series of potential configurations. The climbing-image nudged elastic band (CI-NEB) method[52] is used to obtain the diffusion energy barrier of transition states. The bonding strength is measured with the integration of the bonding and antibonding states between neighboring atoms by projecting the corresponding crystal orbital Hamilton population (COHP)[53] as coded in the Lobster program.[54] To study the adsorption and interactions of molecules, the effect of van der Waals interactions is considered by using the PBE-D2 functional that contains the semi-empirical long-range dispersion correction.[55] The adsorption energy $E_{adsorption}$ is calculated based on the following equation defined as

$$E_{adsorption} = E_{total} - E_{substrate} - E_{molecule} \quad (1)$$

where, E_{total} represents the total energy of the system, $E_{substrate}$ and $E_{molecule}$ refers to the single-point energies of the catalyst substrate and adsorbed molecules, respectively.

3. Results and Discussion

3.1. Hydrogenation Catalysis

A typical Chevrel-phase metal sulfide $NiMo_3S_4$ is chosen as the catalyst for hydrogenation. It is known that the electrocatalysis performance of materials usually depends on the orientation of the crystal planes. Previous studies on $NiMo_3S_4$ for water splitting have demonstrated that the H_2O molecules on the (001)

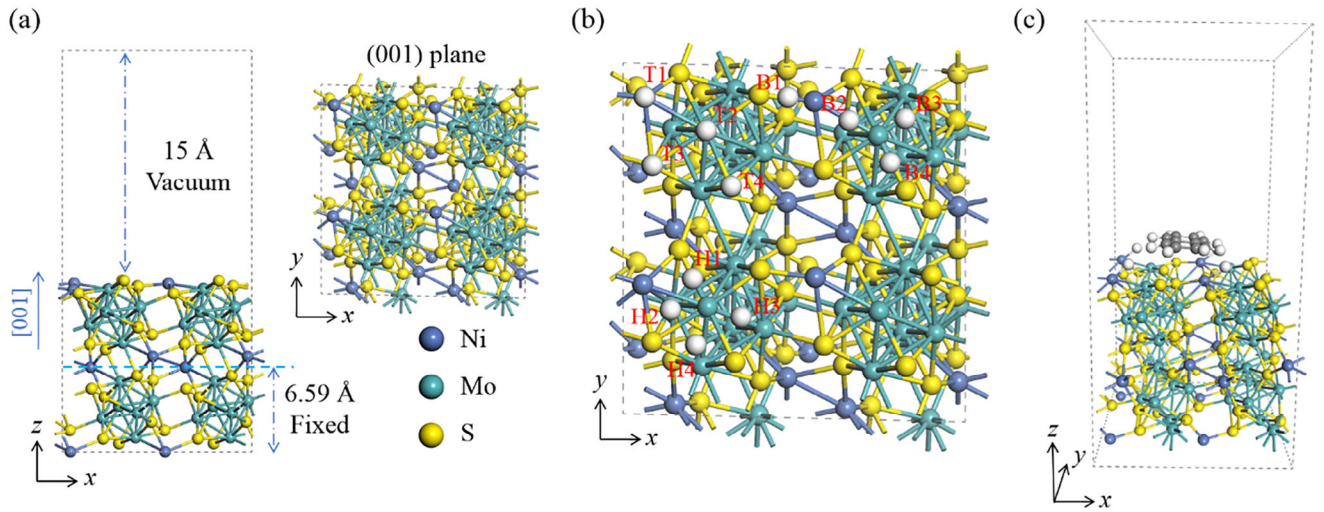

Figure 2. Hydrogenation catalyst model and reactant adsorption sites. a) Optimized slab model of the $NiMo_3S_4$ (001) surface, b) possible adsorption sites for a single H atom, and c) most favorable adsorption configuration of naphthalene molecule and H atoms on the $NiMo_3S_4$(001) catalyst.

surface are more active and experience lower energy barriers for water dissociation as compared to other lattice planes.[32] In addition, the synthesis of 3D laminar $NiMo_3S_4$ has proved that the growth and observation of the (001) surface are more feasible.[29] Therefore, we select the (001) surface for hydrogenation. The corresponding slab model is shown in **Figure 2**a, where the atoms in the bottom five atomic layers with a thickness of 6.59 Å are fixed at their bulk positions, while all the atoms in the top layers are allowed to be fully optimized. The optimized lattice parameters are $a = 12.83$ Å, $b = 13.14$ Å, $c = 27.20$ Å, $\alpha = \beta = 90°$, and $\gamma = 91.40°$.

It is important to note that although naphthalene[24] is a benzene-like planar molecule in which carbon atoms are all sp^2-hybridized forming a closed conjugated configuration, the carbon bond length and internal electron cloud density near the α- and β-site in naphthalene are not homogeneously distributed. Our calculated results show that the adsorption energy of naphthalene on the catalyst of $NiMo_3S_4$(001) surface is −0.63 eV. Such a weak binding mainly results from the uneven surface of the $NiMo_3S_4$(001) substrate, which prevents close contact with the planar naphthalene, despite the naphthalene molecule possessing many unoccupied electronic orbitals perpendicular to the molecular plane in the benzene ring.[56]

Once naphthalene is adsorbed on $NiMo_3S_4$(001) under the atmosphere of saturated hydrogen gas, the hydrogenation stage begins. To understand the mechanism, it is necessary to figure out the distribution tendency of H atoms on the $NiMo_3S_4$(001) substrate. Thus, we first explore the adsorption behavior of a single H atom. As shown in Figure 2b, the nonequivalent possible adsorption sites can be classified into three categories: the top site (S_T) on the top of atoms, the hollow site (S_H) above the center of the atomic rings, and the bridge site (S_B) over the atomic bonds. To check the stability of each adsorption site, we compare their adsorption energy values. Our calculated results show that the energetically most favorable adsorption site is the hollow site S_{H2} with an adsorption energy of −2.25 eV. Thus far, the most favorable adsorption states of the naphthalene molecule and H atoms on the $NiMo_3S_4$(001) catalyst are decided and shown in Figure 2c.

Next, we study the entire hydrogenation process from naphthalene to tetralin in detail. Considering the geometric and electronic structure of naphthalene, we design a total of 12 possible hydrogenation routes, as shown in **Figure 3**a, then calculate and compare the performance of two representative paths by plotting them as energy step diagrams in Figure 3b. At the beginning of hydrogenation, according to the geometric symmetry and uneven charge distribution between the α- and β-site electron cloud densities, the first step would occur on either the α- or β-site in one of the benzene rings. We have found that the energy change of the system is less and the reaction energy barrier is lower when hydrogenating the α-site (0.19 eV) compared to that of the β-site (0.42 eV), hence the first step for naphthalene is easier to occur at the α-site. Thus, excluding the other six pathways starting from the β-site. This is because the electron cloud density at the α-site is higher, making it easier to bind H atoms for hydrogenation. As for the second step of hydrogenation, it would be desirable to form a conjugated relationship between the new hydrogenation site and the existing system. Therefore, after hydrogenating the 1α-site, the options are left for 2β- or 4α-site. We calculate their corresponding energy barriers, respectively, and find that the barrier of attacking the 4α-site (0.25 eV) is lower than that of the 2β-site (0.32 eV). This suggests that, for naphthalene molecules with planar symmetry, H atoms tend to saturate the symmetric sites resulting from the first step during the second hydrogenation step, which maximizes the symmetry of the molecular system. Therefore, the most favorable hydrogenation site for the second step is another α-site in a symmetric position, excluding the feasibility of other geometrical asymmetric paths. In the third step of hydrogenation, the β-sites that are more difficult to be hydrogenated have been activated due to the influence of neighboring α-site hydrogenation. Therefore, although the hydrogenation energy barrier is slightly higher for the 2β-site (0.64 eV), it is comparable with the value of 0.49 eV for the subsequent α-site hydrogenation in other pathways. Through the overall

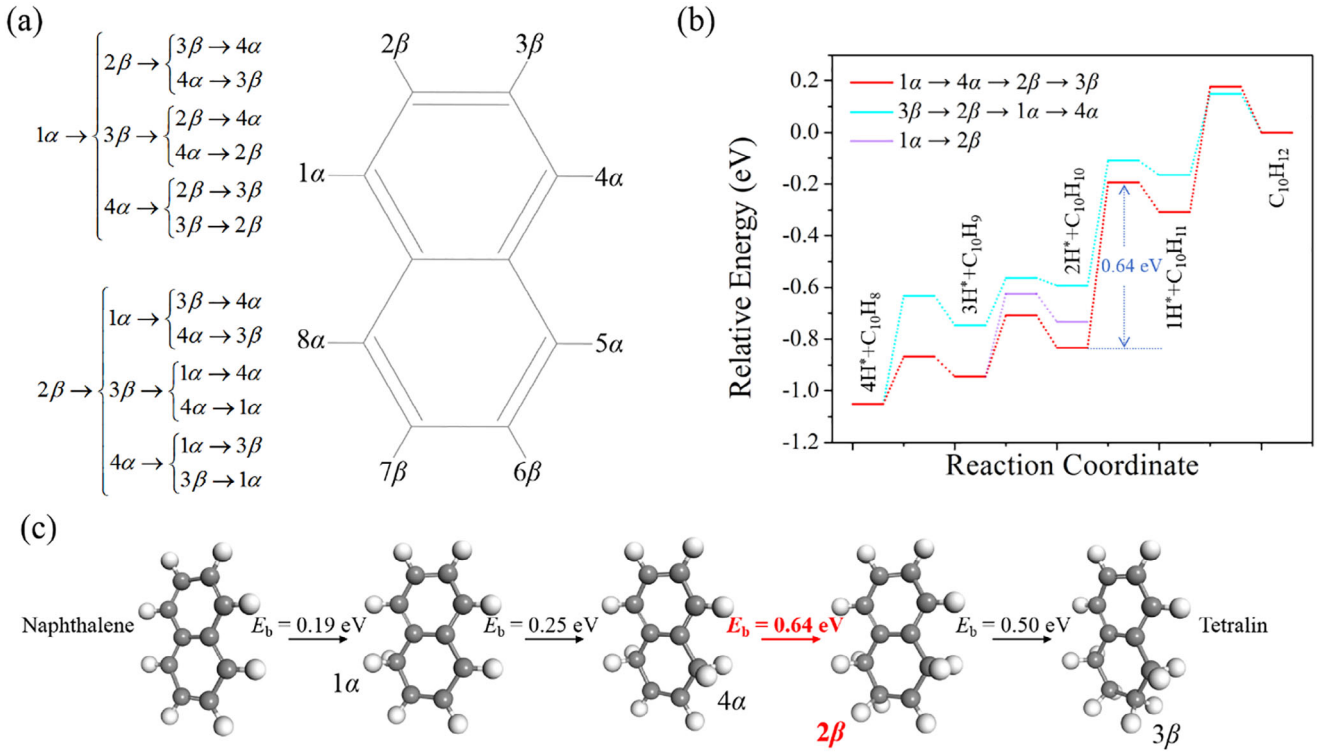

Figure 3. Identification of optimal hydrogenation path for tetralin. a) All potential hydrogenation sequences and corresponding hydrogenation sites. b) Hydrogenation energy step graphs of naphthalene to tetralin: red lines for the optimal steps of $1\alpha \rightarrow 4\alpha \rightarrow 2\beta \rightarrow 3\beta$, blue lines for the compared sequence of $3\beta \rightarrow 2\beta \rightarrow 1\alpha \rightarrow 4\alpha$, and purple step for the comparison of the second step between $1\alpha \rightarrow 4\alpha$ and $1\alpha \rightarrow 2\beta$. c) Sketch of the hydrogenating naphthalene to tetralin and the red arrow is for the rate-determining step.

comparison of the energy barrier for each step, one can see that this step is the rate-determining step in the hydrogenation process. This finding agrees with the previously reported hydrogenation/dehydrogenation pattern for the benzene ring in other polycyclic aromatic hydrocarbons. For example, the hydrogenation of 10H-N-ethylcarbazole (NEC) to 12H-NCE is identified as the rate-determining step[57] and the dehydrogenation from 3H-NEC to 2H-NEC is the specific rate-determining step.[56] The fourth step of hydrogenation still follows the principle of maintaining system symmetry, so the hydrogenation occurs at the other symmetrical site of the previous hydrogenation site. By considering the catalytic energy barrier, overall energy change, and system symmetry requirement, we have finally identified the optimal hydrogenation pathway: $1\alpha \rightarrow 4\alpha \rightarrow 2\beta \rightarrow 3\beta$ site with the third stage as the rate-determining step. Although previous research has reported the reaction conditions[6] and tetralin selectivity,[7] it is difficult to observe such specific hydrogenated intermediates in the experiment, while our theoretical analysis can provide some insight for bridging this gap. It can be seen that the energy of the step diagram shows an overall increasing trend in the entire hydrogenation process. This is because the original unoccupied p_z orbitals perpendicular to the benzene ring plane are gradually filled with electrons from H atoms. The unavailability of interacting with the substrate through *p-d* hybridization weakens the binding between the molecule and the catalytic substrate, resulting in the overall energy of the system showing an upward trend, similar to the case of the hydrogenation in N-ethylcarbazole.[57]

The schematic hydrogenation sequence is shown in Figure 3c and corresponding step-by-step hydrogenation images with the catalytic substrate are presented in Figure S1 (Supporting Information).

3.2. Catalytic Cracking Mechanism

To study the cracking mechanism of the hydrogenation product tetralin, we select the ZSM-5 zeolite[38] as the catalyst, which belongs to aluminosilicate with a pristine chemical composition of $Si_{96}O_{192}$, where the acidic catalytic centers can be activated by introducing Al atoms to the system.[58] We choose the (010) plane for cracking tetralin due to the following reasons: 1) The controllable synthesis of ZSM-5 with the (010) crystal plane has been reported.[59] 2) The (010) surface has a layered configuration, providing more suitable sites for the adsorption and reaction of tetralin.[60] 3) The strength and distribution of acidic sites play a crucial role in the cracking reactions, and previous theoretical studies have shown that the overall performance of acidity on the (010) surface is better than the others.[61]

Accordingly, we build a slab model for the (010) surface of the ZSM-5 catalyst. As shown in **Figure 4a**, where the atoms in the bottom five atomic layers (in the thickness of 6.5 Å) are fixed at the bulk positions of ZSM-5, while the atoms in the top five atomic layers are fully optimized. The optimized lattice parameters are a = 20.09 Å, b = 13.14 Å, c = 29.92 Å, and

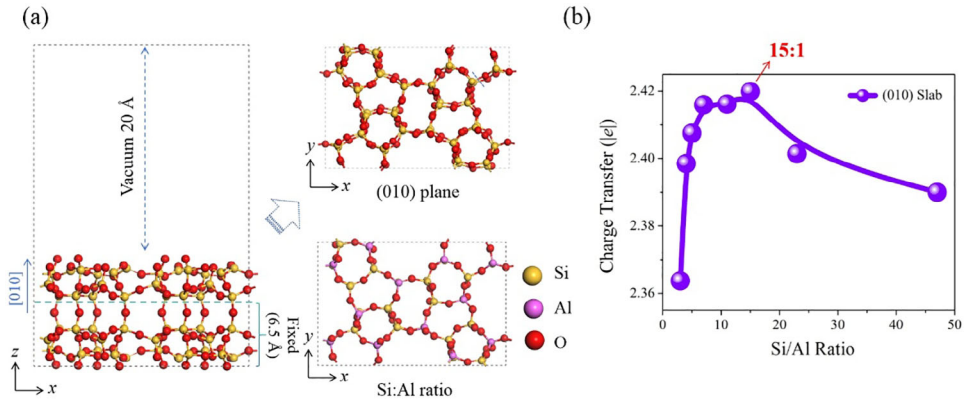

Figure 4. Cracking catalyst and acidity determined the Si/Al ratio. a) Optimized slab model of the ZSM-5 (010) surface and possible Al-doped configurations. b) Variation of transferred charge from the doped Al atoms to the substrate with Si/Al ratio.

$\alpha = \beta = \gamma = 90°$. To determine the doping concentration of Al in the ZSM-5 catalyst, we take different Si/Al composition ratios and calculate the charge transfer from the dopant to the substrate based on Bader charge analysis.[62] According to the findings[63] carbon chains break up at the position where the protonation of carbon occurs in the cracking reactions, and it is more favorable to form a carbocation when more charges are transferred from the dopant Al atom to the substrate. The calculated charge transfer at different Si/Al ratios is plotted in Figure 4b. One can see that when the Si/Al ratio is 15:1, most charges are transferred from the doped Al atom to the substrate, activating the acid center. As the Si/Al ratio increases, the number of acid centers resulting from the dopant Al will decrease. Therefore, considering both the strength and number of acid centers, we set the Si/Al ratio to be 15:1. To determine the ground state atomic configuration with this component ratio, we use the Ewald energy method[50,51] to generate a series of possible configurations and compare their relative energies after geometry optimizations. The stable and metastable structures are given in Figure S2 (Supporting Information).

Using the slab model, we find two favorable adsorption sites in tetralin molecules on the cracking catalyst with adsorption energies of −1.38 and −1.25 eV, respectively, as depicted in Figure S3 (Supporting Information), showing that the adsorption is much stronger than that of naphthalene (−0.63 eV) and tetralin (−0.13 eV) on the surface of hydrogenation catalysts, making it feasible for the hydrogenated molecules to desorb from metal catalyst to Al-doped ZSM-5 surface so that to continue subsequent cracking reactions. We conduct the Bader charge analysis[62] on the carbon atoms in the six-membered cyclohexane carbon ring of the most stably adsorbed tetralin molecules, and corresponding results are shown in **Figure** 5a. The main reason for the asymmetric distribution of charges on such symmetrical molecules is the influence of the cracking catalytic substrate. We find that the largest

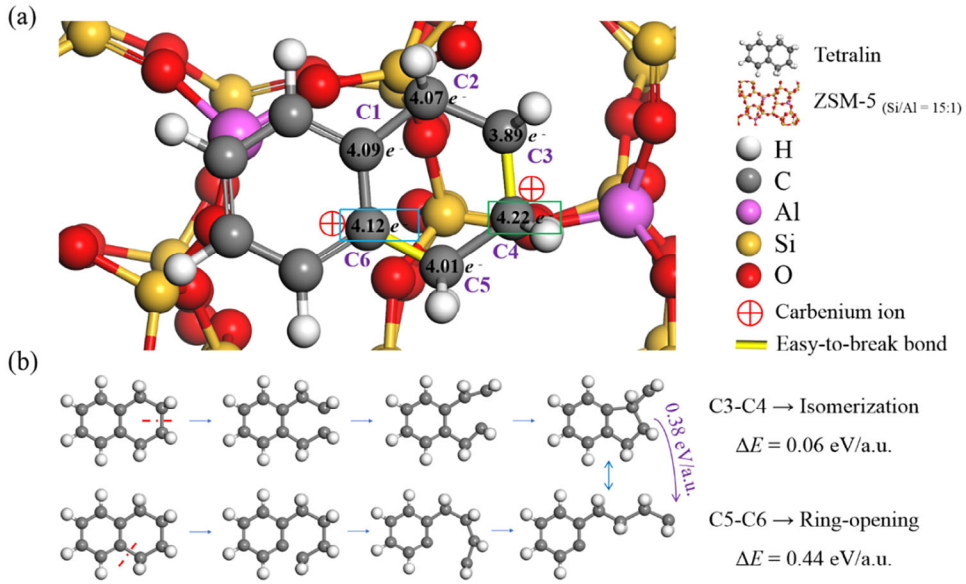

Figure 5. Tetralin adsorption and cracking process. a) Charge distribution and yellow highlighted easy-to-break bonds of adsorbed tetralin and b) two specific cracking processes of C3–C4 or C5–C6 bond breaking for isomerization or ring-opening reaction, respectively.

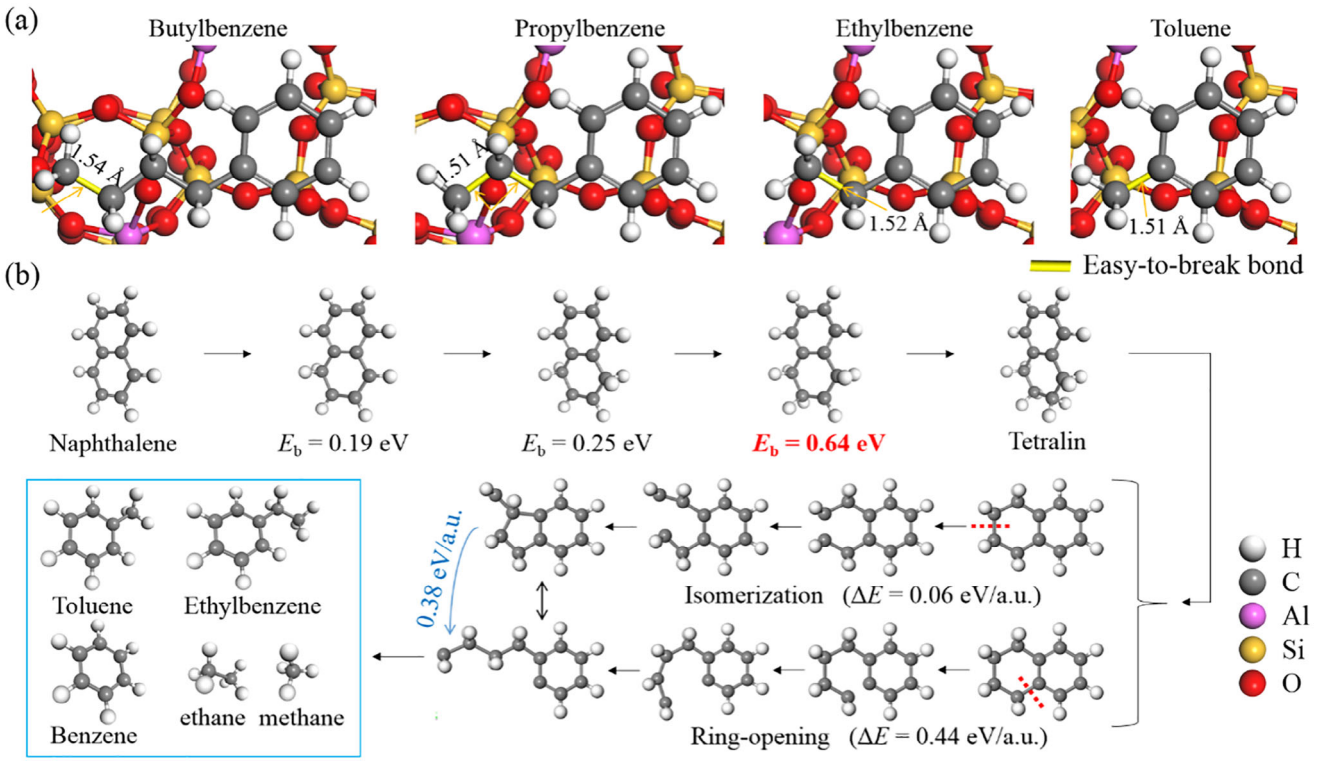

Figure 6. Hydrocracking process of naphthalene and main products. a) Molecular structures of cracking intermediates with highlighted easy-to-break bonds after ring-opening reaction. b) Schematic diagram of an entire hydrocracking process of naphthalene and its main products.

difference in charge is on the carbon atoms at the β-position (in the green box) and the junctional position (in the blue box) with their nearby carbon atoms, so these two atoms will become carbenium ions when contacting with the acidic centers on the cracking catalyst. The Coulomb repulsion between the charged C atoms weakens the strength of the bond. The bond length analysis of carbon atoms also proves the feasibility of bond breaking where the two carbon bonds highlighted with yellow possess a length of ≈1.56 Å, much longer than the average values of 1.4 Å of carbon bonds in the benzene ring and 1.5 Å of carbon bonds in the cyclohexane ring. To further study the bonding strength between the C atoms in the hexagonal cyclohexane carbon rings, we perform the projected COHP calculation[53] with the results presented in Figure S4 (Supporting Information), where the positive side of the curve represents the bonding contribution and the negative side refers to the antibonding contribution. The integral value of the COHP curve can be seen as the number of bonded electrons shared by the two C atoms, i.e. larger absolute value indicates stronger bond strength. The calculated integral values of COHP curves for C3–C4 and C5–C6 bonds are −5.73 and −5.99 eV, respectively, and their absolute values are less than that of C1–C2 (−6.35 eV), C2–C3 (−6.84 eV), and C4–C5 (−6.84 eV) bonds, also implying that the C3–C4 and C5–C6 bonds are much easier to be broken than other ones. After geometrically optimizing the structures with these two kinds of broken bonds, we find that they spontaneously form two types of cracking intermediates due to the influence of the catalyst substrate and the elemental characteristics. As shown in Figure 5b, when the carbon bond of C3–C4 breaks, the original six-membered carbon ring changes into a five-membered ring with a side chain. When the carbon bond of C5–C6 breaks, the original hexagonal carbon ring converts into a long chain. Both two situations have been observed in experiments, and have been proven to be the reversible reaction between each other.[64] To further investigate the relationship between these two cracking reactions, we calculate the energy changes in the system in producing these two intermediates. It is found that when a ring-opening reaction occurs, the energy of the system further decreases by 0.38 eV/a.u. The details are shown in Figure S5 (Supporting Information). In terms of energetics, the ring-opening reaction resulting from the fracture of the C5–C6 bond is relatively favorable to occur, indicating that the tendency is more likely toward the ring-opening direction in the reversible reaction even if the system has undergone the isomerization. However, due to larger polarity difference, longer carbon bond length, and weaker bond strength, the C3–C4 bond is more prone to break, making the isomerization reaction much easier to occur. Therefore, these two reactions would proceed simultaneously to generate more ring-opened intermediates.

3.3. Hydrocracking Products

The hydrogenation reaction occurs continuously in the H_2 atmosphere until all unsaturated bonds are fully hydrogenated. The cracking reaction would also occur on the generated side chains until all the carbon bonds become difficult to break or only the isolated benzene ring is left. Based on the mechanisms of hydrogenation and cracking processes discussed above, the following

reaction process can be derived from the analysis of the charge distribution, bond length, and interaction strength of carbon atoms on the generated side chains. The alkylbenzene directly resulting from the ring-opening reaction is the butylbenzene with its outermost C atom on the side chain easier to break, producing propylbenzene and methane. The outermost and second outermost C atoms on the side chain of propylbenzene both possess a tendency to break, bringing the intermediates of ethylbenzene, toluene, methane, and ethane. Similarly, the cracking of the side carbon chain would also be possible to happen on ethylbenzene and toluene, and every easy-to-break bond of each intermediate is highlighted in their adsorbed molecular structure diagram as presented in **Figure** 6a. Thus, the main products of naphthalene in hydrocracking catalytic reaction are found to be toluene, ethylbenzene, benzene, ethane, and methane, as shown in Figure 6b. They all belong to the BTEX family and are consistent with the results reported recently in industry and experiment.[65]

4. Conclusion

In summary, we have studied the reaction mechanisms and main products of naphthalene during the hydrocracking process over the $NiMo_3S_4$ and ZSM-5 catalysts. The $NiMo_3S_4$ (001) surface is chosen to be the hydrogenation catalyst due to its high catalytic activity and the advantages in growth. The optimal reaction pathway for the hydrogenation of naphthalene to tetralin is identified as $1\alpha \rightarrow 4\alpha \rightarrow 2\beta \rightarrow 3\beta$ with the third one as the rate-determining step. Compared with other pathways, this one not only has energetic superiority but also maintains the symmetry of the reactant system. The (010) surface of ZSM-5 is selected as the cracking catalyst due to its favorable acidity and growth feasibility. The cracking process of tetralin is found to involve breaking carbon bonds with weaker bonding, isomerization, and ring-opening. The simulation-derived main products of naphthalene after hydrocracking are toluene, ethylbenzene, benzene, ethane, and methane, consistent with the experimental results reported for the BTEX family. This work provides theoretical insights into the primary reaction mechanisms of the naphthalene hydrocracking process, which would motivate further research on efficient hydrocracking of polycyclic aromatic hydrocarbons in heavy oil.

Supporting Information

Supporting Information is available from the Wiley Online Library or from the author.

Acknowledgements

This work is supported by the China National Petroleum Corporation-Peking University Strategic Cooperation Project of Fundamental Research and National Natural Science Foundation of China (Grants No. NSFC-12274007). It is also supported by the high-performance computing platform of Peking University, China.

Conflict of Interest

The authors declare no conflict of interest.

Data Availability Statement

The data that support the findings of this study are available in the supplementary material of this article.

Keywords

density functional theory, hydrocracking reaction, naphthalene, $NiMo_3S_4$/ZSM-5 catalyst, tetralin

Received: February 5, 2025
Revised: April 16, 2025
Published online: May 27, 2025

[1] F. Chen, G. Zhang, X. Weng, Y. Zhang, L. Zhao, L. Cao, J. Gao, C. Xu, X. Liu, X. Gao, *Appl. Catal., A* **2021**, *616*, 118095.
[2] R. Saab, K. Polychronopoulou, L. Zheng, S. Kumar, A. Schiffer, *J. Ind. Eng. Chem.* **2020**, *89*, 83.
[3] C. Peng, X. Huang, X. Duan, Z. Cheng, R. Zeng, R. Guo, X. Fang, *Catal. Today* **2016**, *271*, 149.
[4] M. Ebrahiminejad, R. Karimzadeh, *Adv. Powder Technol.* **2019**, *30*, 1450.
[5] H. Ma, X. Yang, G. Wen, G. Tian, L. Wang, Y. Xu, B. Wang, Z. Tian, L. Lin, *Catal. Lett.* **2007**, *116*, 149.
[6] X. Liu, K. J. Smith, *Appl. Catal., A* **2008**, *335*, 230.
[7] S. Ardakani, K. J. Smith, *Appl. Catal., A* **2011**, *403*, 36.
[8] S. G. A. Ferraz, B. M. Santos, F. M. Z. Zotin, L. R. R. Araujo, J. L. Zotin, *Ind. Eng. Chem. Res.* **2015**, *54*, 2646.
[9] D. P. Upare, S. Park, M. S. Kim, J. Kim, D. Lee, J. Lee, H. Chang, W. Choi, S. Choi, Y.-P. Jeon, Y.-K. Park, C. W. Lee, *J. Ind. Eng. Chem.* **2016**, *35*, 99.
[10] J. Chen, C. Peng, X. Fang, Z. Zhou, *CIESC J.* **2018**, *69*, 709.
[11] Y. Kim, K. Cho, Y. Lee, *J. Catal.* **2017**, *351*, 67.
[12] N. H. R. Annuar, S. Triwahyono, A. A. Jalil, N. Basar, T. A. T. Abdullah, A. Ahmad, *Appl. Catal., A* **2017**, *541*, 77.
[13] D. P. Upare, S. Park, M. S. Kim, Y.-P. Jeon, J. Kim, D. Lee, J. Lee, H. Chang, S. Choi, W. Choi, Y.-K. Park, C. W. Lee, *J. Ind. Eng. Chem.* **2017**, *46*, 356.
[14] N. Jin, G. Wang, L. Yao, M. Hu, J. Gao, *Ind. Eng. Chem. Res.* **2016**, *55*, 5108.
[15] N. Zhang, J. Ma, R. Li, H. Jiao, *ACS Catal.* **2020**, *10*, 9215.
[16] S. Akmaz, P. A. Caglayan, *Chem. Eng. Technol.* **2015**, *38*, 917.
[17] S. C. Korre, M. T. Klein, R. J. Quann, *Ind. Eng. Chem. Res.* **1997**, *36*, 2041.
[18] A. Corma, V. González-Alfaro, A. V. Orchillés, *J. Catal.* **2001**, *200*, 34.
[19] H. Jia, B. Chen, G. Zhang, W. Yan, W. Hao, J. Ma, R. Li, *Appl. Catal., O* **2024**, *193*, 206974.
[20] H. Yang, W. Huang, D. Chen, H. Liu, M. Huang, Z. Xu, Y. Zhou, Q. Wei, *Appl. Catal., A* **2024**, *685*, 119880.
[21] K. Sato, Y. Iwata, Y. Miki, H. Shimada, *J. Catal.* **1999**, *186*, 45.
[22] L. Piccolo, S. Nassreddine, G. Toussaint, C. Geantet, *ChemSusChem* **2012**, *5*, 1717.
[23] H. Jia, W. Yan, Q. Dong, B. Qing, W. Hao, Y. Du, X. Zhang, J. Ma, R. Li, *J. Energy Inst.* **2024**, *116*, 101716.
[24] L. F. Fieser, W. C. Lothrop, *J. Am. Chem. Soc.* **1935**, *57*, 1459.
[25] D. Hu, A. Duan, C. Xu, P. Zheng, Y. Li, C. Xiao, C. Liu, Q. Meng, H. Li, *Nanoscale* **2019**, *11*, 15519.
[26] M. A. Lukowski, A. S. Daniel, F. Meng, A. Forticaux, L. Li, S. Jin, *J. Am. Chem. Soc.* **2013**, *135*, 10274.
[27] S. Zhang, B. V. R. Chowdari, Z. Wen, J. Jin, J. Yang, *ACS Nano* **2015**, *9*, 12464.

[28] J. Zheng, K. Lebedev, S. Wu, C. Huang, T. Ayvalı, T. Wu, Y. Li, P. Ho, Y. Soo, A. Kirkland, S. C. E. Tsang, *J. Am. Chem. Soc.* **2021**, *143*, 7979.
[29] D. Kong, Y. Wang, Y. V. Lim, S. Huang, J. Zhang, B. Liu, T. Chen, H. Y. Yang, *Nano Energy* **2018**, *49*, 460.
[30] Y. Wang, X. Li, M. Zhang, J. Zhang, Z. Chen, X. Zheng, Z. Tian, N. Zhao, X. Han, K. Zaghib, Y. Wang, Y. Deng, W. Hu, *Adv. Mater.* **2022**, *34*, 2107053.
[31] D. Kong, Y. Wang, S. Huang, Y. V. Lim, M. Wang, T. Xu, J. Zang, X. Li, H. Y. Yang, *J. Colloid Interface Sci.* **2022**, *607*, 1876.
[32] S. Chandrasekaran, T. Ma, Z. Hu, Q. Liu, C. Zhan, Y. Li, C. Bowen, H. Lu, Y. Liu, *Appl. Catal., B* **2023**, *338*, 123007.
[33] J. Jiang, M. Gao, W. Sheng, Y. Yan, *Angew. Chem., Int. Ed.* **2016**, *55*, 15240.
[34] Y. Choi, J. Lee, J. Shin, S. Lee, D. Kim, J. K. Lee, *Appl. Catal., A* **2015**, *492*, 140.
[35] A. Bhan, E. Iglesia, *Acc. Chem. Res.* **2008**, *41*, 559.
[36] D. L. Jurković, A. Kostyniuk, B. Likozar, *Chem. Eng. J.* **2022**, *445*, 136898.
[37] R. Khare, D. Millar, A. Bhan, *J. Catal.* **2015**, *321*, 23.
[38] T. Pan, S. Ge, M. Yu, Y. Ju, R. Zhang, P. Wu, K. Zhou, Z. Wu, *Fuel* **2022**, *311*, 122629.
[39] J. P. Marques, I. Gener, P. Ayrault, J. C. Bordado, J. M. Lopes, F. R. Ribeiro, M. Guisnet, *Microporous Mesoporous Mater.* **2003**, *60*, 251.
[40] X. Song, Q. Guan, Z. Cheng, W. Li, *Appl. Catal., B* **2018**, *227*, 13.
[41] S. R. Kirumakki, B. G. Shpeizer, G. V. Sagar, K. V. R. Chary, A. Clearfield, *J. Catal.* **2016**, *242*, 319.
[42] W. W. McNeary, S. A. Tacey, G. D. Lahti, D. R. Conklin, K. A. Unocic, E. C. D. Tan, E. C. Wegener, T. E. Erden, S. Moulton, C. Gump, J. Burger, M. B. Griffin, C. A. Farberow, M. J. Watson, L. Tuxworth, K. M. V. Allsburg, A. A. Dameron, K. Buechler, D. R. Vardon, *ACS Catal.* **2021**, *11*, 8538.
[43] P. E. Blöchl, *Phys. Rev. B* **1994**, *50*, 17953.
[44] G. Kresse, D. Joubert, *Phys. Rev. B* **1999**, *59*, 1758.
[45] G. Kresse, J. Furthmüller, *Phys. Rev. B* **1996**, *54*, 11169.
[46] M. P. Teter, M. C. Payne, D. C. Allan, *Phys. Rev. B* **1989**, *40*, 12255.
[47] J. P. Perdew, K. Burke, M. Ernzerhof, *Phys. Rev. Lett.* **1996**, *77*, 3865.
[48] H. J. Monkhorst, J. D. Pack, *Phys. Rev. B* **1976**, *13*, 5188.
[49] A. Jain, S. P. Ong, G. Hautier, W. Chen, W. D. Richards, S. Dacek, S. Cholia, D. Gunter, D. Skinner, G. Ceder, K. A. Persson, *APL Mater.* **2013**, *1*, 011002.
[50] S. P. Ong, W. D. Richards, A. Jain, G. Hautier, M. Kocher, S. Cholia, D. Gunter, V. L. Chevrier, K. A. Persson, G. Ceder, *Comput. Mater. Sci.* **2013**, *68*, 314.
[51] S. Wang, Q. Bai, A. M. Nolan, Y. Liu, S. Gong, Q. Sun, Y. Mo, *Angew. Chem., Int. Ed.* **2019**, *58*, 8039.
[52] G. Mills, H. J´onsson, *Phys. Rev. Lett.* **1994**, *72*, 1124.
[53] V. L. Deringer, A. L. Tchougréeff, R. Dronskowski, *J. Phys. Chem. A* **2011**, *115*, 5461.
[54] R. Nelson, C. Ertural, J. George, V. L. Deringer, G. Hautier, R. Dronskowski, *J. Comput. Chem.* **2020**, *41*, 1931.
[55] S. Grimme, *J. Comput. Chem.* **2006**, *27*, 1787.
[56] Z. Zhang, T. Liu, X. Zhang, C. Zhang, X. Jin, J. Zheng, Q. Sun, *ACS Appl. Mater. Interfaces* **2024**, *16*, 37963.
[57] H. Yu, Z. Zhang, X. Jin, X. Zhang, R. Jin, Y. Lin, Z. Xie, Y. Huang, T. Liu, X. Li, Q. Sun, J. Zheng, *ACS Catal.* **2024**, *14*, 10519.
[58] M. Ravi, V. L. Sushkevich, J. A. van Bokhoven, *Nat. Mater.* **2020**, *19*, 1047.
[59] M. Choi, K. Na, J. Kim, Y. Sakamoto, O. Terasaki, R. Ryoo, *Nature* **2009**, *461*, 246.
[60] H. Wang, Y. Hou, W. Sun, Q. Hu, H. Xiong, T. Wang, B. Yan, W. Qian, *ACS Catal.* **2020**, *10*, 5288.
[61] L. Treps, A. Gomez, T. de Bruin, C. Chizallet, *ACS Catal.* **2020**, *10*, 3297.
[62] W. Tang, E. Sanville, G. Henkelman, *J. Phys.: Condens. Matter* **2009**, *21*, 084204.
[63] J. Wang, S. Ding, S. Peng, Z. Yang, Y. Du, *RSC Adv.* **2022**, *12*, 19537.
[64] C. L. Russell, M. T. Klein, R. J. Quann, J. Trewella, *Energy Fuels* **1994**, *8*, 1394.
[65] X. Su, P. An, J. Gao, R. Wang, Y. Zhang, X. Li, Y. Zhao, Y. Liu, X. Ma, M. Sun, *Chin. J. Chem. Eng.* **2020**, *28*, 2566.